Preprint typeset in JINST style - HYPER VERSION

Shielding Design for the ISODAR Neutrino Experiment

arXiv:1909.08009v1 [physics.acc-ph] 17 Sep 2019

Adriana Bungau[a], Jose Alonso[a], Larry Bartoszek[b c], Janet M. Conrad[a], Edward Dunton[b], Michael H. Shaevitz[b]

[a] *Massachusetts Institute of Technology, Cambridge, MA 02139, USA*
[b] *Columbia University, New York, NY 10027, USA*
[c] *Bartoszek Engineering, 818 W. Downer Place, Aurora, IL 60506-4904, USA*

E-mail: abungau@mit.edu

ABSTRACT: The IsoDAR sterile-neutrino search requires a very high intensity neutrino source. For IsoDAR, this high intensity is produced using the high neutron flux from a 60 MeV, 10 mA proton beam striking a beryllium target that floods a sleeve of highly-enriched Li-7. Through neutron capture the Li-7 is transmuted to Li-8, which beta-decays giving the desired high neutrino flux for very-short baseline neutrino experiments. The target can be placed very close to can existing large neutrino detector, which is typically located deep underground to reduce backgrounds. With such a setup, it is necessary to design a shielding enclosure for the target to prevent neutrons from causing unacceptable activation of the rock walls close to the target. Various materials have been studied including steel to thermalize the high energy neutrons and two new types of concrete developed by Jefferson Laboratory, one very light with shredded plastic aggregate, and the other one enriched with high quantities of boron. The shielding is asymmetrical, having a larger thickness towards the detector in order to suppress the neutron and gamma background in the neutrino detector. Simulation results for rock activation and for detector backgrounds are presented.

KEYWORDS: IsoDAR; DAEDALUS; Shielding..

Contents

1. General Considerations **2**

2. The IsoDAR Experiment **2**
2.1 The IsoDAR Design 3
2.2 The IsoDAR Shielding 3

3. Shielding Considerations **4**
3.1 Neutron Flux Limitation 4
3.2 Shielding Materials 4

4. Monte Carlo Simulations **5**
4.1 The Physics Model 5
4.2 Validation Studies 6

5. Shielding Design **8**
5.1 Material Performance 8
5.2 Design Optimisation 12

6. Rock Activation Studies **13**
6.1 Methodology for Calculation of Induced Activity 14
6.2 KamLAND Rock Composition 15
6.3 List of Radionuclides Produced 16
6.4 Spatial Distribution of Activity Induced at Various Depths 17
6.5 Activity induced in the rock 19
6.6 Distribution of Isotope Production with Rock Height 19

7. Shielding Requirements for Reducing the Neutron and Photon Physics Backgrounds in the KamLAND Detector **22**
7.1 Neutron Shielding 22
7.1.1 Target Shielding 22
7.1.2 Additional Shielding Design 23
7.1.3 KamLAND Buffer Region and Additional Shielding 23
7.2 Photon background 25

8. Conclusion **27**

1. General Considerations

The shielding design for high energy facilities and particle accelerators has become a key aspect of radiation protection due to the deep penetration of high energy neutrons. Protection against neutron radiation is obtained by using appropriate thicknesses and proper types of shielding materials that will slow down the high energy neutrons in the first stage and then absorb the slow neutrons in the second stage to reduce the neutron radiation to acceptable levels. The IsoDAR experiment, in combination with KamLAND detector in Japan [1], will perform sensitive short-baseline neutrino oscillation searches and electro-weak measurements associated with beyond-the-standard-model physics. The requirements for shielding and radiation protection, according to Japanese law, must be in conformance with IAEA recommendations [2]. In accordance with these requirements, the rock activation of the cavern wall due to artificially produced radionuclides must not exceed 0.1 Bq/g. The radiation exposure will be maintained as low as reasonably achievable through shielding around the beam-dump neutrino source. The effectiveness of the shielding will be actively monitored by radiation instruments located in the control room and by frequent area-surveys performed by health physics personnel. Additional shielding is also required to reduce the unwanted neutron and gamma interactions in the KamLAND detector that could cause significant backgrounds for the physics measurements.

This paper is organised as follows. Section 2 describes the conceptual design of the IsoDAR system as outlined in the Conceptual Design Report [3] [4]. Shielding considerations regarding the neutron flux limitations, rock analysis and shielding material choice and combinations are presented in Section 3. The Monte Carlo simulations and validation with experimental data and MCNPX (Monte Carlo N-Particle eXtended) studies follow in Chapter 4. Material performance and design optimization are presented in section 5. The simulation results of rock activation and radionuclides produced are discussed in Section 6 while the results for neutron and photon background estimates in KamLAND detector are presented in Section 7.

2. The IsoDAR Experiment

At present, the particle physics community is placing a high priority on investigating neutrino masses, oscillations, and mixings [5, 6]. Although in the 3-neutrino oscillation model the three mixing angles and masses associated with three standard neutrino flavors are relatively well known, anomalous results have been observed at LSND [7], MiniBooNE [8] and short-baseline reactor experiments [9]. These inconsistencies can be explained with the hypothesis of a (3+N) sterile neutrino model in which there are three light neutrino mass states and N more massive sterile neutrino states. IsoDAR is a proposed neutrino experiment that is being developed to do a definitive search for sterile neutrinos in the ~ 1 eV^2 Δm^2 mass region.

The IsoDAR experimental program will produce a high intensity $\bar{\nu}_e$ beam from the β^- decay of ^{8}Li. The $\bar{\nu}_e$ can interact in the detector via the inverse beta decay (IBD) process: $\bar{\nu}_e + p \rightarrow e^+ + n$. In addition, IsoDAR also represents an important technological step, in terms of producing high-power cyclotrons that can be used for a number of physics and non-physics applications [10], [11], [12].

2.1 The IsoDAR Design

The IsoDAR conceptual design consists of an ion source which injects up to 50 mA of H2+ into a high-power cyclotron that is required to capture and accelerate up to 5 mA of H2+ ions up to 60 MeV/ amu. Immediately after extraction, the molecular H2+ is dissociated into two protons, with 10 mA of protons delivered to the target system. The ^{9}Be target will produce a high neutron flux that will then enter a sleeve surrounding the target, which contains 99.995% pure ^{7}Li (Fig. 1). The neutron capture on ^{7}Li will create ^{8}Li isotopes which will then beta decay producing the electron antineutrinos. In the conceptual design the sleeve material is a mixture of lithium-floride and beryllium-floride (FLiBe), but recent studies have shown that a homogeneous mixture of lithium and beryllium with an optimum beryllium fraction mass of 75% has a better efficiency of production of ^{8}Li yield [13]. The system is enclosed in a graphite reflector to enhance the neutron capture on ^{7}Li. When coupled with the KamLAND detector, IsoDAR will observe 8.2×10^{5} reconstructed IBD events in five years of 90% duty factor running. With this data set, IsoDAR will provide 5σ sensitivity to sterile neutrino oscillation models as well as allow precision measurements of $\bar{\nu}_e - e$ scattering and searches for the production and decay of exotic particles [14].

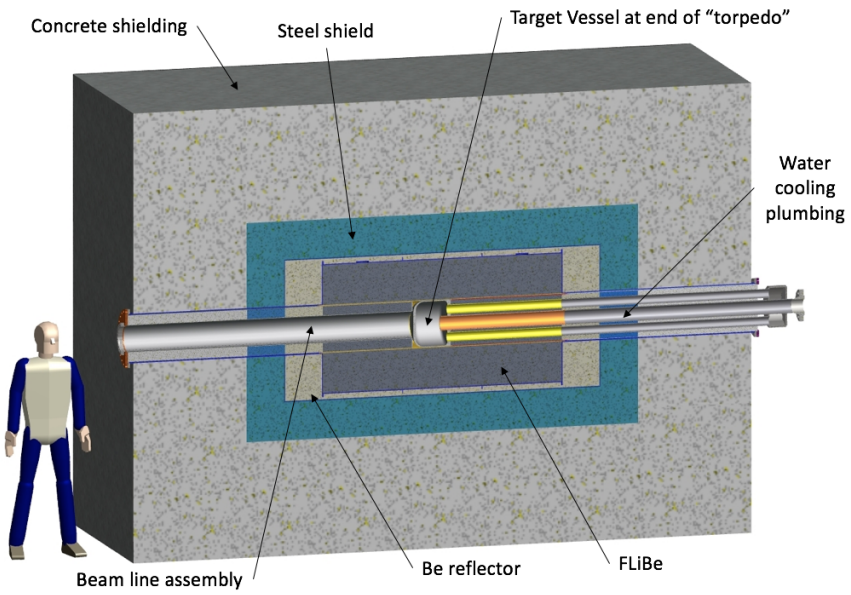


Figure 1. The current layout of the target and shielding system. The target torpedo is surrounded by LiBe sleeve (dark grey) and by graphite reflector (grey). The target system is enclosed in shielding (steel and concrete mixtures).

2.2 The IsoDAR Shielding

The target assembly is to be placed in the Kamioka mine next to the 1 kton KamLAND liquid scintillator neutrino detector in one of the current utility areas near the detector. The space in this area will have approximate cross section dimensions of 2.25 m floor to ceiling and 3.5 m side to side. The remaining space after placing the target system will be used for shielding. Preliminary

calculations indicated that this space will need to be enlarged, particularly in the vertical direction. Minor excavation of the mine is allowed if it can be accomplished without blasting. At the front and back end of the target system, extra shielding material can be added if required.

3. Shielding Considerations

In the shielding design two types of radiation need to be considered: neutrons and gamma rays. Most materials can attenuate gamma rays as the thickness is increased with the higher the atomic number and higher density of material giving greater the attenuation. The total neutron flux that is produced in the target system during the experiment depends on the target and sleeve geometries and their materials. A large fraction of these neutrons will be low energy neutrons. Other neutrons reaching the cavern walls could also come from beam loss in the cyclotron and transport line to the target, but this can be minimized by reducing beam losses and providing active monitors that interrupt the beam when abnormally high neutron levels are detected. Additional shielding will be used to reduce the irradiation from the flux produced from unavoidable beam loss.

3.1 Neutron Flux Limitation

The neutrons that escape the shielding around the target will produce rock activation in the cavern walls. Radionuclides with half-lives shorter than days, or even months, are of no consequence, but the progenitors of long-lived products (i.e. ^{60}Co, ^{152}Eu, ^{154}Eu, ^{134}Cs etc.) need to be assessed. Rock samples were collected from various sites in the mine in close proximity to the experiment location, and were irradiated in the reactor at MIT with a flux of $10^{18} n/cm^2$. An analysis of the irradiated samples was performed at MIT and at LBNL and determined the presence of cobalt and europium at the parts-per-million levels. As progenitors of ^{152}Eu, ^{154}Eu and ^{60}Co these concentrations provide a measure of the upper limit of allowed neutron flux to exit the outer surface of the shielding. From these measurements and calculations, a limit is set at $10^{-13} n/p/mm^2$ neutrons into the cavern walls.

3.2 Shielding Materials

The KamLAND detector is a delicate and sensitive large detection instrument and any mining activity in the close proximity of the detector needs to be minimized. Therefore, minimizing the total volume of rock that must be removed for the IsoDAR target cavern is a prime requirement, which can be accomplished with the careful selection of target shielding material. The choice of shielding is strongly dependent on neutron energy, so an efficient combination of materials must shield against the entire range of neutron energies. There are several factors that must be taken into account when selecting the shielding materials. Considerations such as effectiveness, strength, resistance to damage and cost efficiency can affect radiation protection in many ways. While metals are strong and resistant to radiation damage, they undergo changes in their mechanical properties and degrade in time from radiation exposure. On the other hand, concrete materials are strong, durable and cost effective however they are weaker at elevated temperatures and less effective at blocking neutrons. The materials used in this study were selected from a set of compound materials taking into account radiation shielding performance, physical and thermal properties and cost.

First, the fast neutrons must be slowed down via inelastic scattering by using appropriate metal based attenuation materials like iron (carbon steel or stainless steel). Once the neutrons are slowed down to thermal energies by inelastic collisions, then in a second stage the thermal neutrons are captured by the absorbing material. Low-Z materials containing a high fraction of hydrogen (for example water, plastic, concrete) can provide good neutron energy attenuation as a result of elastic scattering of neutrons on protons. At these neutron energies the interaction cross section is high and the energy lost in a collision is significant. However, water is not a reliable candidate as it can evaporate and leak while plastic materials are expensive. Concrete is a good candidate as it is inexpensive and combines many of the good aspects required for shielding, particularly when different materials can be added as aggregates to the mixture. The Jefferson Laboratory (JLab) recently developed new shielding materials, a plastic concrete which performs better than other materials for neutron thermalisation and a boron rich concrete which absorbs neutrons using less material [15].
By adding shredded plastic which contains more hydrogen atoms to the concrete, one can increase its ability to thermalise neutrons while decreasing its weight. Also, by removing the grit and rocks that are normally found in concrete to make it even lighter, the plastic concrete is basically two thirds of the weight of the normal concrete and four times better at thermalising neutrons. The boron rich concrete is basically Portland cement in which the normal rock/sand aggregate is replaced by pelletised boron carbide. In concrete, the neutrons are thermalised when they strike hydrogen atoms in the water molecules that are trapped during the concrete mixing process. Boron has a high neutron capture cross section and has been generally used in for neutrino shielding in addition to concrete. The final product is a much better absorber and has the same consistency as ordinary concrete and several layers of boron concrete were used in our studies. In summary, the current IsoDAR shielding consists of a combination of high-Z and low-Z materials which satisfies the requirements mentioned above.

4. Monte Carlo Simulations

4.1 The Physics Model

There are several Monte Carlo simulation packages used for shielding calculations and, for the calculations of the efficiency and performance of the shielding materials described in this paper, the Geant4 simulation program was used [1]. The Geant4 modelling included the geometrical setup described before and the corresponding material properties, as well as the characteristics of the incoming proton beam.

The physics package *particle_hp* was used in the current shielding simulations, which comprises a set of hadronic models for proton and neutron inelastic interactions for an energy range up to 200 MeV. The package works with Geant4 versions *geant4.9.5* and later and uses evaluated nuclear data bases for inelastic interactions of proton, neutron, deuteron, triton, He3, alpha and gamma. *Particle_hp* includes three physics lists: one for protons *QGSP_BIC_PHP*, one for neutrons *QGSP_BIC_NHP*, and one for all particles, i.e. neutrons, protons, deuterons, tritons, He3,

[1]More information on the Geant4 physics models can be found in the Physics Reference Manual: http://cern.ch/geant4/UserDocumentation/UsersGuides/ PhysicsReferenceManual/html/PhysicsReferenceManual.html.

alpha and gamma, *QGSP_BIC_AllHP*. The abbreviation QGSP stands for the Quark Gluon String Parton model, BIC for the Binary Intranuclear Cascade and HP for the high-precision neutron package which includes evaluated neutron data for neutron interactions below 20 MeV. The last two physics lists give the same results for neutrons as the physics list *QGSP_BIC_HP*. The evaluated nuclear data libraries differ and, thus, the results of the Monte Carlo simulations will depend on the library. Two databases *ENDF/B-VII.1* [16] and *TENDL-2014* [17] were used for cross sections of primary and secondary particle interactions. The *ENDF/B-VII.1* library uses experimental data for projectile energies up to 150 MeV, which are essentially nuclear reaction cross sections together with the distribution in energy and angle of the secondary reaction products. Also, it contains data only for 49 isotopes, including Be. The *TENDL-2014* library uses some experimental data and *TALYS* [18] calculations for projectile energies up to 200 MeV. It contains information for all isotopes and can be applied to all target materials but the best results are obtained for targets with atomic number in the range 12-289. For neutron energies below 20 MeV, the high-precision model is employed, which uses *ENDF/B-VII.1*, JENDL [19], MENDL-2 [20] and other data libraries [21]. The Binary Intranuclear Cascade model is called for neutron energies above 20 MeV. This model includes a low energy nuclear de-excitation model called the G4Precompound model which is called by the simulation when the particle energy is below 100 MeV and when the nuclear structure effects start to play an important role.

4.2 Validation Studies

Differential neutron yields for several angles and various beam energies were measured in References [22]-[28]. New measurements of the neutron yield produced by a 62 MeV proton beam on a thick beryllium target were performed at Laboratori Nazionali del Sud (LNS) of INFN using the existing superconducting cyclotron [29]. A 62 MeV proton beam with an operating beam current of 30-50 pA was extracted from the cyclotron and transported through the beam transport system to the target. The beryllium target had a thickness of 3 cm and 3.5 cm diameter. This thickness was chosen to ensure complete absorption of the protons. The neutrons produced in the target were measured by the time-of-flight technique. Eight neutron detectors were installed around the target, at the same height with respect to the beamline, with different angles and with two different distances (150 cm and 75 cm). The electric charge deposited by the beam on the target was measured by a digital current integrator and used for absolute normalization of the data.

The target and the detector set up were modelled in the Geant4 simulations. The *particle_hp* physics package was used to simulate the neutron yield produced by 62 MeV protons and Fig. 2 shows the results at 0°, 30°, 90° and 150°. The comparison of the simulation with the experimental data taken from this experiment and also from Refs. [22], [23], and [24] at 0° for lower beam energies shows a significant disagreement in the lower neutron energy range. This disagreement demonstrates lower beam energy data cannot be extrapolated to higher beam energies simply by an overall factor since the kinematic limits have to be taken into account. For low energy neutrons (below 10 MeV) there is a disagreement between data and simulation especially at lower angles. The *ENDF VII* database library for particle cross sections was released in December 2011 and therefore it does not contain the experimental results measured in Ref. [29] at the later date. However, at larger angles, there is a good agreement between these two, even for low energy neutrons (above 2 MeV). At larger angles (150°) there is a good agreement between the measured data in

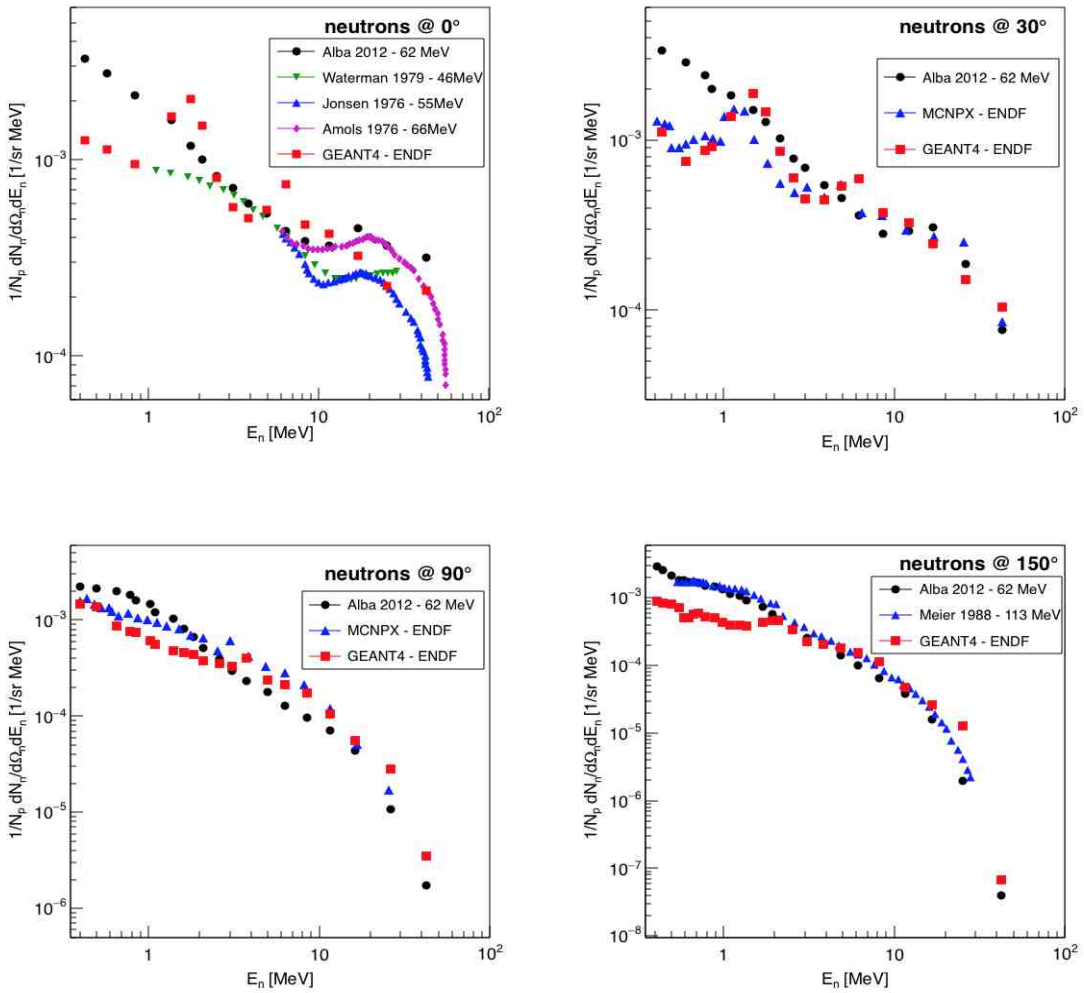


Figure 2. Comparison of the *particle_hp* physics package predictions with the experimental data taken from this experiment, Ref. [2-5] and MCNPX simulations. The neutron yield was measured at 0°, 30°, 90° and 150°. The proton energy is 62 MeV in all the Geant4 simulations.

this experiment and Ref. [25] with the Geant4 code predictions for neutron energies above 2 MeV. At neutron energies below 1-2 MeV, the Geant4 predictions lie below the data. However these low energy neutrons will not make it through the shielding and therefore will not pose a problem for the rock activation studies.

The Geant4 simulations were then compared with MCNPX results [31] using the ENDF data library for the measured cross sections. The comparison shows good agreement between the predictions of the two codes at larger angles, 30° and 90°. There is a good agreement between the two codes and the data in some kinematic regions at larger angles and larger neutron energies.

The experimental measurements in ref. [29] which are not included in the ENDF/B-VII proton database, show a difference about a factor of two greater than the values obtained with the two simulation packages below 1-2 MeV. However simulation values are higher in the range 2-70 MeV,

so overall we expect the experimental and simulated neutron yields values integrated over the entire energy range (1-70 MeV), to be similar. This has been shown to be indeed the case in the validation study [13] performed against the experimental measurements of neutron fluxes published in Ref. [30].

As more experimental data for protons on beryllium become available, they will be added to the proton ENDF database increasing the accuracy of the model predictions. The current predictions of the *particle_hp* model rely on the existing tabulated experimental data and will improve as the new data is implemented. The validation studies shown above as well as previous studies of 60 MeV protons on beryllium [13] have shown that the *particle_hp* model with the ENDF data library describes the proton inelastic interactions on Be for 60 MeV incident energy better than any other theoretical model available justifying its selection for these studies.

5. Shielding Design

5.1 Material Performance

Simulations were carried out to asses the performance of the selected shielding materials. Neutron shielding materials with variable thickness placed in different arrangements were examined and the comparisons are shown in this section. As the area where the target system and the surrounding shielding will be located was once a construction tunnel for KamLAND, its dimensions are not overly generous. The cross section of the cavern which measures roughly 2.3 m high by 3.5 m wide leaves ≈50 cm from the target system to the ceiling. As the available vertical space is the critical dimension in our Monte Carlo modelling, the figure of merit in the simulations is the neutron flux recorded on the ceiling, at 90 degrees with respect to the beam direction. Initial studies using inner layers of plastic concrete for neutron moderation and outer layers of boron rich concrete for neutron absorption for the available ∼50 cm showed that the neutron flux was several orders of magnitude higher than the desired value of $10^{-13} n/p/mm^2$. These results implied that rock will need to be removed to place an adequately shielded target in this tunnel. A summary of all the materials combinations, total shielding thickness and the neutron flux obtained in the simulations is shown in Table 1.

Table 1. The materials combinations and the total shielding thickness used in the simulations.

Materials Combinations	Total thickness	Neutron flux
plastic concrete and boron loaded concrete	100 cm	above $\Phi = 10^{-13} n/p/mm^2$
20 cm steel, plastic concrete and boron loaded concrete	120 cm	some below $\Phi = 10^{-13} n/p/mm^2$
steel and boron loaded concrete	120 cm	some below $\Phi = 10^{-13} n/p/mm^2$
steel and boron loaded concrete	200 cm	below $\Phi = 10^{-13} n/p/mm^2$

Assuming that a minimum of 50 cm of rock will be removed from the cavern ceiling, a target shielding of total thickness of maximum 100 cm of various combinations of plastic concrete and

boron rich concrete was considered. The thickness of each material layer was 10 cm in our simulations. The neutron flux recorded at 90 degrees on a detector sphere was still above the desired value, $10^{-13} n/p/mm^2$ (Fig. 3). This was due to the fact that the fast neutrons would escape the 100 cm of shielding and suggesting thus that more high-Z material is required to attenuate them. The inelastic scattering on high-Z atoms will reduce the neutron energy to a much lower value such that they will be absorbed in the boron rich concrete layers. Therefore, in addition to the 100 cm shielding of plastic concrete and boron rich concrete, two layers of 20 cm total thickness of steel were added. In this configuration, the inner layers are steel, followed by variable thicknesses of plastic concrete. The outer layers are boron rich concrete to absorb the neutrons. The results are shown in Fig. 4.

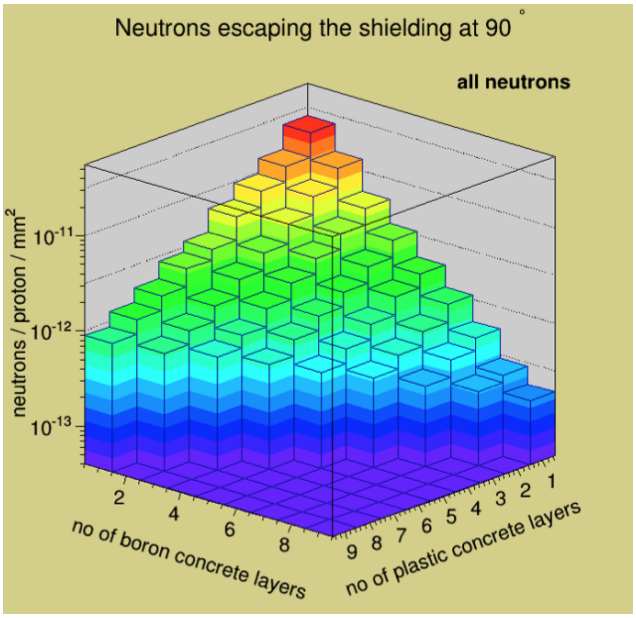


Figure 3. The neutron flux escaping the shielding at a 90 degrees angle with respect to the proton beam direction. The shielding consists of combinations of layers of plastic concrete and boron rich concrete, each layer being 10 cm thick. The total shielding thickness is up to 100 cm. The neutron flux is above the desired value $10^{-13} n/p/mm^2$ for all combinations. (The purple combinations are not considered since they have total thicknesses greater than 100 cm.)

There are several material combinations for which the neutron flux is lower than $10^{-13} n/p/mm^2$ (left plot). The flux is lowest for the combination 20 cm steel, 10 cm plastic concrete and 90 cm boron rich concrete. As Fig. 4 suggests, the optimum solution is for a minimum thickness of plastic concrete and indicates that better results can be obtained for combinations of steel and boron rich concrete only. The same total shielding thickness of 120 cm was maintained but plastic concrete was removed completely. The results are shown in Fig. 5. The neutron flux can be brought down to $10^{-15} n/p/mm^2$ for 90 cm of steel and 30 cm of boron concrete. Because of the cost and total shielding weight, a final baseline configuration of 30 cm of steel and 90 cm of boron rich concrete was selected. The total mass of the baseline target system and shielding from this study comes to 165,331 kg.

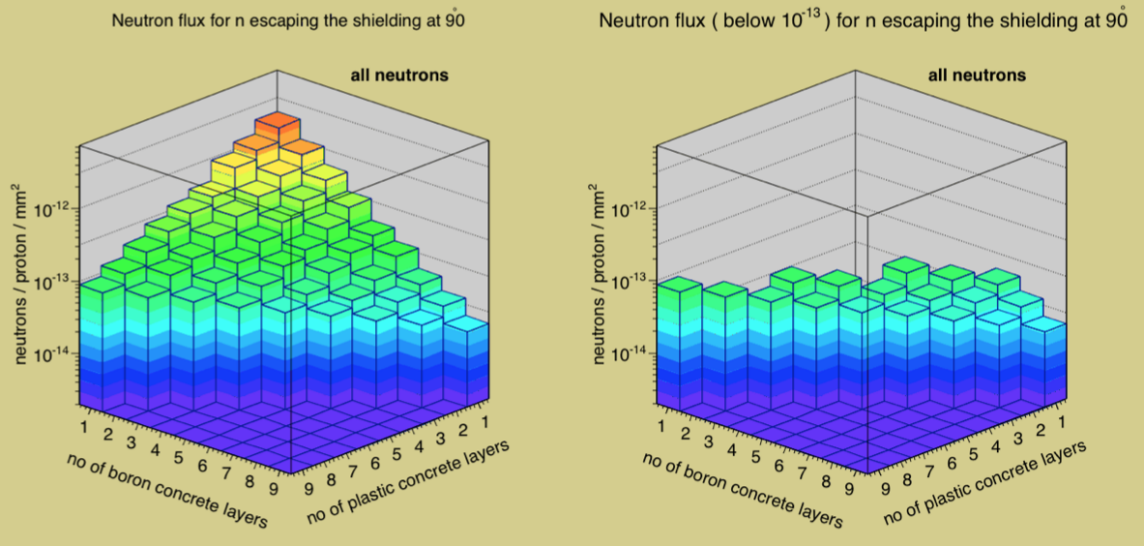


Figure 4. The neutron flux out of the shielding at 90 degrees with respect to the beam direction. The shielding consists of two inner layers of steel of 20 cm total thickness (not shown), followed by combinations of layers of plastic concrete and boron rich concrete (left plot). Each layer has 10 cm thickness and the total shielding thickness is up to 120 cm. The right plot shows only those combinations for which the neutron flux is below the desired value $10^{-13} n/p/mm^2$.

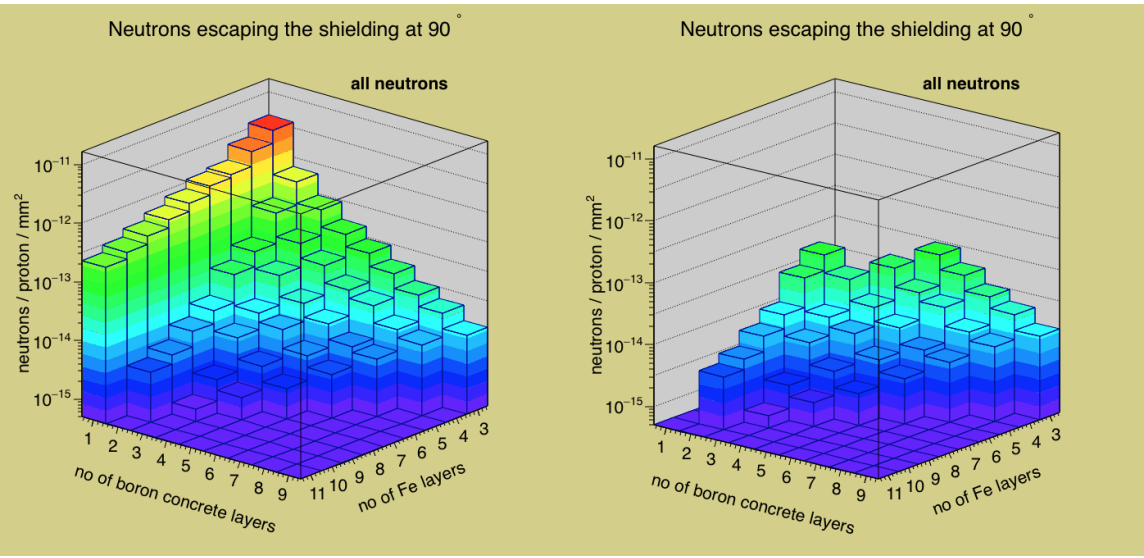


Figure 5. The neutron flux escaping the shielding at 90 degrees with respect to the beam direction, using only combinations of layers of steel and boron concrete, but no plastic concrete. Each layer is 10 cm thick and the total thickness is up to 120 cm (left plot). For some combinations, the flux is much lower in this case than when plastic concrete was present and lower than the desired value $10^{-13} n/p/mm^2$ (right plot).

The neutron flux for this particular shielding configuration (30 cm steel and 90 cm boron rich concrete) was recorded on a detector sphere of radius 3.5 m and the results are shown in Fig. 6. The beam travels from right to left in Fig. 6. The lower flux values at 40 and 140 degrees correspond

to the corners of the concrete shielding block and the higher values of flux above 140 degrees correspond to neutrons escaping into the space left for the wobbler magnets in front of the target where additional shielding can be placed (see comment below). The average neutron flux at 90 degrees for all energies is 1.88 $\times 10^{-15} n/p/mm^2$. Of greatest interest in this study is the flux at 90 degrees, or neutrons penetrating through the thinnest point of the bulk shielding. It should be noted from Fig. 6 that there is an appreciable number of neutrons at 0 and 180 degrees that escape the shielding block. The very high 'wings' at low and high angles point to holes in the shielding for beam entry and target servicing. As seen below, addition of more shielding both upstream and downstream can adequately control these higher fluxes. As distance along the axis of the beam does not impact cavern size, such additions have little consequence on the rock excavation question.

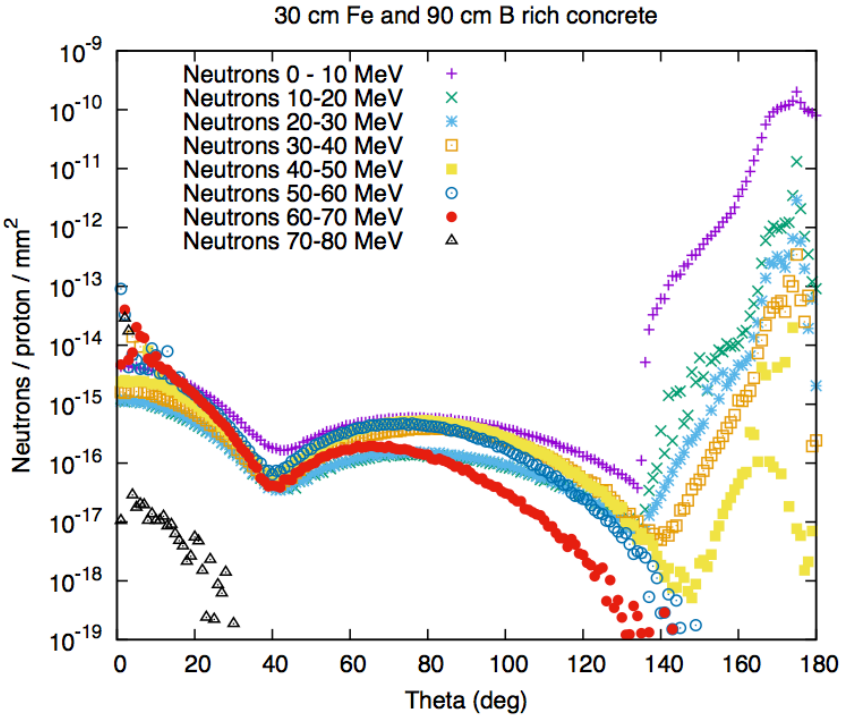


Figure 6. The neutron flux detected on a sphere surrounding the shielding. The sphere radius is 350 cm. The shielding material consists of 30 cm Fe and 90 cm boron rich concrete. The high values of neutron flux at 0 and 180 degrees correspond to holes in the shielding for beam entry and target servicing.

To obtain a more accurate calculation of the neutron flux, simulated detector plates were placed on the shielding block to record the flux at 0, 90 and 180 degrees for this baseline shielding configuration with 30 cm of steel and 90 cm of boron rich concrete. The neutron flux detected at the front and at the back of the shielding block is shown in Fig. 7. The neutron contamination in the proton beam pipe has a peak value of $2.4 \times 10^{-6} n/p/mm^2$ while the flux in the space left for the wobbler magnets has a peak value of $1.4 \times 10^{-6} n/p/mm^2$. The neutron flux detected on the plate

above the shielding block (Fig. 8) is forward biased, as most of the neutrons that are backscattered escape in the space left for the magnets and therefore have no chance to be scattered into the sleeve and detected on the first half of the plate. The average neutron flux is $4\times10^{-11} n/p/mm^2$.

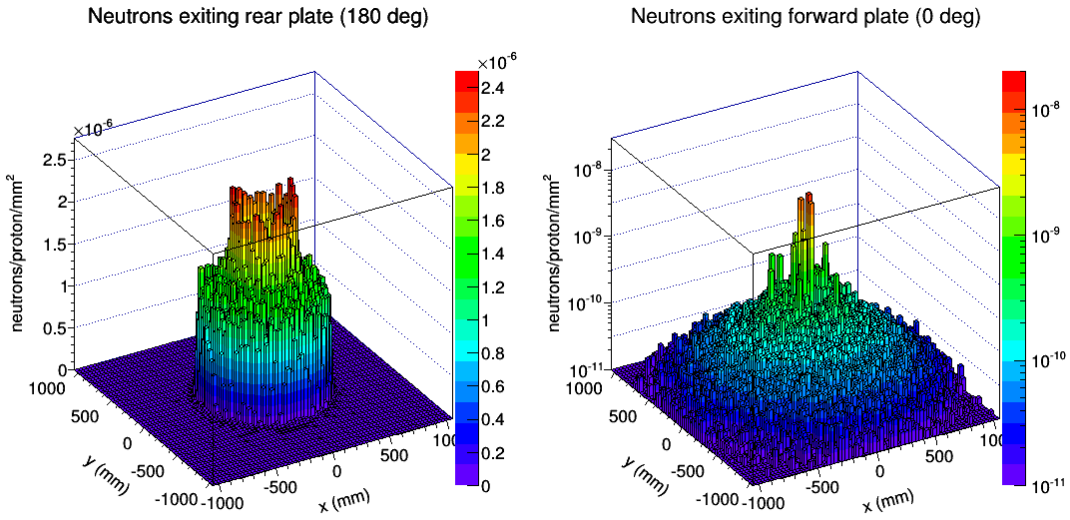


Figure 7. Neutron flux recorded on detector plates placed at 0 and 180 deg on the target shielding. The shielding is made of 30 cm steel and 90 cm boron rich concrete.

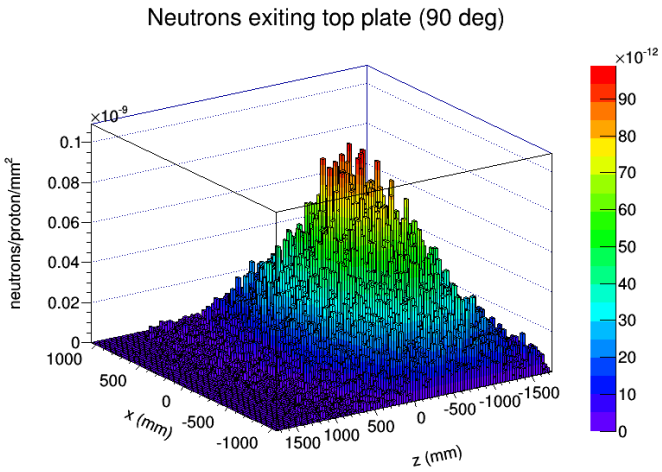


Figure 8. Neutron flux at 90 deg for a shielding consisting of 30 cm steel and 90 cm boron rich concrete. The neutron levels can be translated into rock activation, as shown in the next section.

5.2 Design Optimisation

Slight changes to this design were imposed by the fact that a large fraction of backscattered neutrons escape in the space left for the wobbler magnets without being moderated and captured by

shielding. To avoid this, the hole at the front end of the target system was sealed with shielding, leaving space only for the proton beam pipe. The wobbler magnet will be placed outside the shielding block, as well as the 30 degree bending magnet. This new configuration will adequately block the escaping neutron flux in the upstream direction (Fig. 9). The forward neutron flux (at low angles) can be further attenuated by using movable blocks of steel and concrete. There is much less of a space restriction at the beam height, so added material can be readily provided. This extra material needs to be movable to enable changing of the target assemblies, which occurs from the downstream side of the target complex.

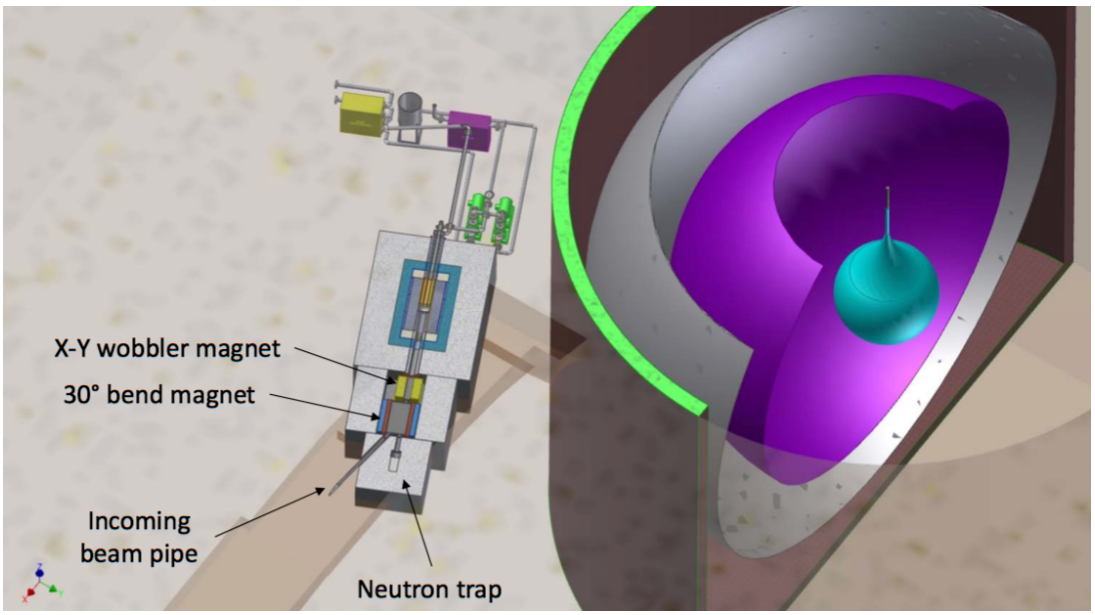


Figure 9. Aerial view of the target and shielding system, with the wobbler magnet and bending magnet placed outside the shielding block. The KamLAND detector with the surrounding buffer region and water layer is also shown.

Figure 10 shows that the neutron flux after optimization (the holes at the front and at the back of the target were filled with shielding material and the new material combination was changed to 40 cm steel and 80 cm boron rich concrete for better neutron attenuation). The neutron flux is much lowered in the optimized design as seen in Fig. 10. The detector sphere radius is 7 m as it surrounds not just the target system but also the wobbler magnet and the neutron trap.

6. Rock Activation Studies

Although the parametric studies of neutron flux versus shielding composition suggested an optimized preliminary design for which the neutron flux was below the desired value, the ultimate shielding effectiveness is given by the rock activation of cavern wall which must not exceed 0.1 Bq/g. Therefore, the calculation of induced activation and the analysis of the radionuclides produced serve as the guide in designing the final shielding configuration.

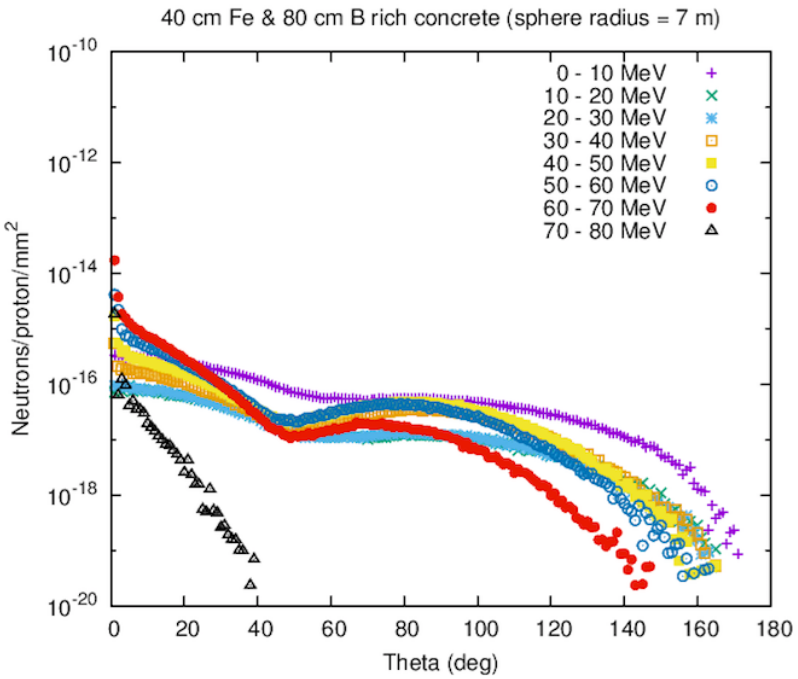


Figure 10. The neutron flux detected on a sphere surrounding the shielding after seal in the space for magnets. The shielding material consists of 40 cm steel and 80 cm boron rich concrete.

6.1 Methodology for Calculation of Induced Activity

The time dependence of the number of radioisotopes produced is given by the individual production and decay rate of each isotope. The production rate for a radioactive isotope is given by:

$$\frac{dN_i^{prod}}{dt} = \frac{N_{iso}}{\Delta t} = \frac{N_{iso} I}{N_p e} \tag{6.1}$$

where N_{iso} is the number of isotopes produced by the simulation, I is the current, N_p is the number of simulated protons, and e is the proton charge. Once the radioisotopes are produced, they decay exponentially with time. The decay rate for each isotope i is a function of its decay constant:

$$\frac{dN_i^{decay}(t)}{dt} = -\lambda_i N_i(t) \tag{6.2}$$

During the beam-on period, the time evolution can be obtained by combining the production and decay rates:

$$\frac{dN_i(t)}{dt} = \frac{N_{iso} I}{N_p e} - \lambda_i N_i(t) \tag{6.3}$$

The solution of Eq. 6.3, gives the number of isotopes at any time t during the beam exposure:

$$N_i(t) = \frac{N_{iso} I}{N_p e \lambda_i}(1 - \exp(-\lambda_i t)) \tag{6.4}$$

However, after the beam is switched off, following a continuous exposure for a time t_1, the number of isotopes after a time t, which includes both the beam on period t_1 as well as a beam off period t_2, is given by:

$$N_i(t) = \frac{N_{iso}I}{N_p e \lambda_i}(1 - \exp(-\lambda_i t_1))\exp(-\lambda_i(t_2)) \tag{6.5}$$

The induced activity given by one particular isotope is given by Eq. 6.6:

$$A_i(t) = \lambda_i N_i(t) \tag{6.6}$$

Using Eq. 6.5 and Eq. 6.6, the activity of each isotope produced can be given at any given time t which includes the beam on time t_1 and the beam off time t_2. The total induced activity given by all isotopes is given by Eq. 6.7:

$$A(t) = \sum_i \lambda_i N_i(t) \tag{6.7}$$

The production rates of all isotopes produced in the rock are required further for calculation of the total induced activity.

6.2 KamLAND Rock Composition

KamLAND is located under the peak of Ikenoyama (Ike Mountain, 36.42°N, 137.31°E). Various types of rocks are found in Ikenoyama in unknown quantities, such as Inishi type rocks, skarn rocks, but also granite and limestone. The Inishi type rock is characteristic for the Japanese mountains and is made of various oxides with a high concentration of SiO_2. Skarns are calcium-bearing silicate rocks that are most often formed at the contact zone between intrusions of granitic magma bodies and carbonate sedimentary rocks such as limestone and dolostone. The skarn-type rock is defined as a combination of 70% granite and 30% limestone. The specific gravity for generic skarn is 2.75% g/cm^3 and for the Inishi rock is 2.65 % g/cm^3 [32]. The exact composition of the Inishi rock is given in Table 2 [33] [34].

Table 2. Chemical composition of the Inishi-type rock in elemental percentage.

Compound	Composition (%)	Compound	Composition (%)
SiO_2	60.70	CaO	6.00
TiO_2	0.31	Na_2O	6.42
Al_2O_3	17.39	K_2O	3.47
Fe_2O_3	1.10	P_2O_5	0.18
FeO	1.22	H_2O	1.27
MnO	0.15	S	0.01
MgO	0.93	CO_2	0.96

6.3 List of Radionuclides Produced

Composition analysis of rock samples collected in the mine and irradiated in the MIT reactor indicated that the rocks contained traces of cobalt and europium. The cobalt concentration in the rock samples varied from 1 to 30 ppm by weight, while europium concentrations averaged around 1 ppm. These element concentrations were taken into account for the above Inishi-rock composition. Geant4 simulations show that the isotopes that are produced in the rock are: ^{7}Be, ^{46}Sc, ^{44}Ti, ^{51}Cr, ^{54}Mn, ^{59}Fe, ^{56}Co, ^{57}Co, ^{58}Co, ^{60}Co, ^{22}Na, ^{152}Eu, ^{154}Eu, ^{134}Eu and ^{134}Cs. (Fig. 11).

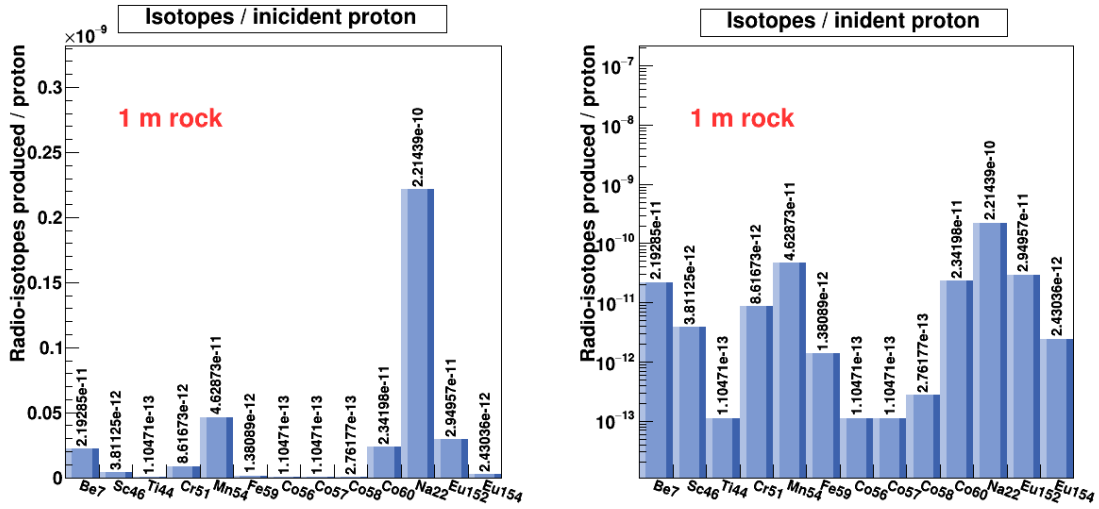


Figure 11. Rate of the isotope production in 1 m of Inishi-type rock. The production rate is dominated by the long-lived isotopes. The shielding consists of 40 cm steel and 80 cm boron concrete.

Many of these isotopes were seen in the MIT activation spectra. One notable not seen is ^{22}Na which has a 13 MeV threshold due to the (n, 2n) production channel. No neutrons at the reactor have this high energy, however the neutron spectrum from the IsoDAR target does have this and higher energies. The majority of these isotopes have a half life of several days, but ^{60}Co, ^{22}Na, ^{152}Eu, and ^{154}Eu dominate the production rate and have a lifetime range between 2.6 - 13.5 years. Also, ^{44}Ti has a lifetime of 63 years, but this isotope was found in small quantities. Table 3 shows the characteristics of the isotopes of interest.

Table 3. Characteristics of the isotopes of interest.

Isotope	Half life	Progenitor	Concentration	Neutron energy	Cross section(barns)
^{60}Co	5.2 y	^{59}Co	30 ppm	Thermal	20
^{152}Eu	13.5 y	^{151}Eu	1 ppm	Thermal	50000
^{154}Eu	8.6 y	^{153}Eu	1 ppm	Thermal	2000
^{22}Na	2.6 y	^{23}Na(n,2n)	5%	>13 MeV	0.015

6.4 Spatial Distribution of Activity Induced at Various Depths

A rock sample having the same area as the top part of the shielding block and a thickness of 100 cm, was considered in our simulations. The rock sample was placed on top of the shielding block in the Monte Carlo modelling. The rock composition is the same as in Table 2 with Co and Eu fractions by weight added. Using the equations above, one can calculate the spatial distribution of induced activity of all isotopes produced at various depths. The rock sample was sliced into 20 layers, each having 5 cm thickness. The total activity is averaged over the entire rock area, however there is a central hot spot in the rock sample where the distribution is approximately uniform and where the activity is averaged over the hot spot size of 100×100 cm. The activity is calculated after 5 years beam on and 2 years beam cool down time for the 40 cm steel and 80 cm boron concrete shielding. Figs. 12 and 13 show the activity in the first 50 cm rock close to the target shielding. The overall activity in the rock is above the required level of 0.1 Bq/g, and much higher on the central hotspots. As most of the isotopes are short lived, the contribution to the total activity after seven years must be associated with the long lived isotopes like ^{60}Co, ^{152}Eu, ^{154}Eu and ^{22}Na. The contribution for these isotopes to the total activity in Bq/g in the central hotspots is shown in Table 4 for all 20 rock layers. The ^{22}Na gives the highest activation and it is produced by the fast neutrons escaping from the shielding, indicating that thicker layers of steel are needed for extra safety.

Table 4. Contribution to the total induced activity of all 13 isotopes in the central hot spots (100 × 100 cm) in Bq/g, given by the long-lived isotopes of interest.

Rock layer (cm)	^{60}Co	^{152}Eu	^{154}Eu	^{22}Na	Total
0-5	0	0	0	0.014	0.053
5-10	0	0.011	0	0.034	0.052
10-15	0.006	0.011	0	0.061	0.069
15-20	0.017	0.021	0	0.007	0.125
20-25	0.040	0.005	0	0.061	0.109
25-30	0.040	0.021	0.005	0.109	0.151
30-35	0.063	0.021	0	0.143	0.208
35-40	0.046	0.043	0	0.232	0.238
40-45	0.069	0.048	0.005	0.348	0.356
45-50	0.063	0.043	0.005	0.286	0.437
50-55	0.155	0.048	0	0.354	0.500
55-60	0.115	0.064	0.005	0.423	0.823
60-65	0.126	0.101	0.016	0.682	0.935
65-70	0.143	0.069	0	0.791	0.986
70-75	0.138	0.080	0	1.070	1.370
75-80	0.092	0.080	0.011	1.360	1.620
80-85	0.109	0.112	0.005	1.830	2.040
85-90	0.149	0.085	0	1.960	2.580
90-95	0.080	0.053	0.011	2.840	3.460
95-100	0.063	0.016	0.005	3.550	4.070

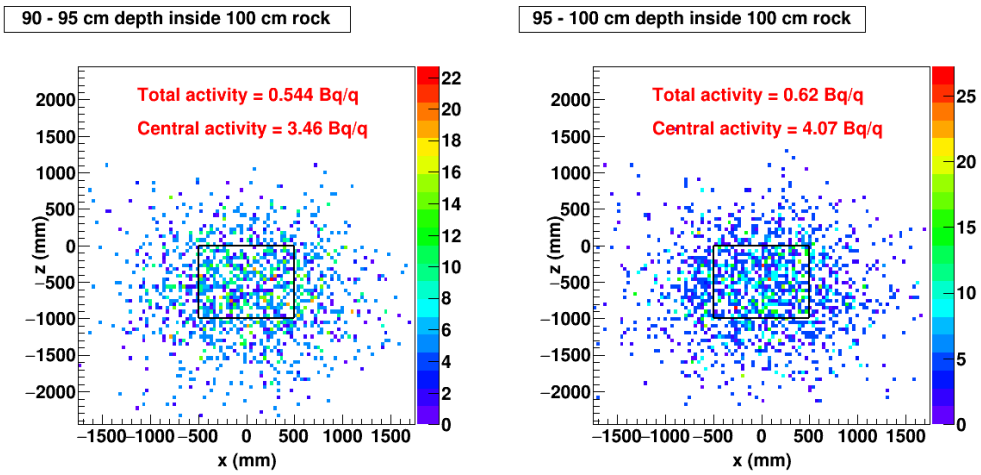


Figure 12. Spatial distribution of induced activity in the lowest layers of the considered rock sample, in the close proximity of the target and shielding system (90-100 cm). The overall activity in the layers is above the required limit of 0.1 Bq/g and much higher in the central hotspots. This analysis is for the 40 cm steel and 80 cm boron concrete shielding.

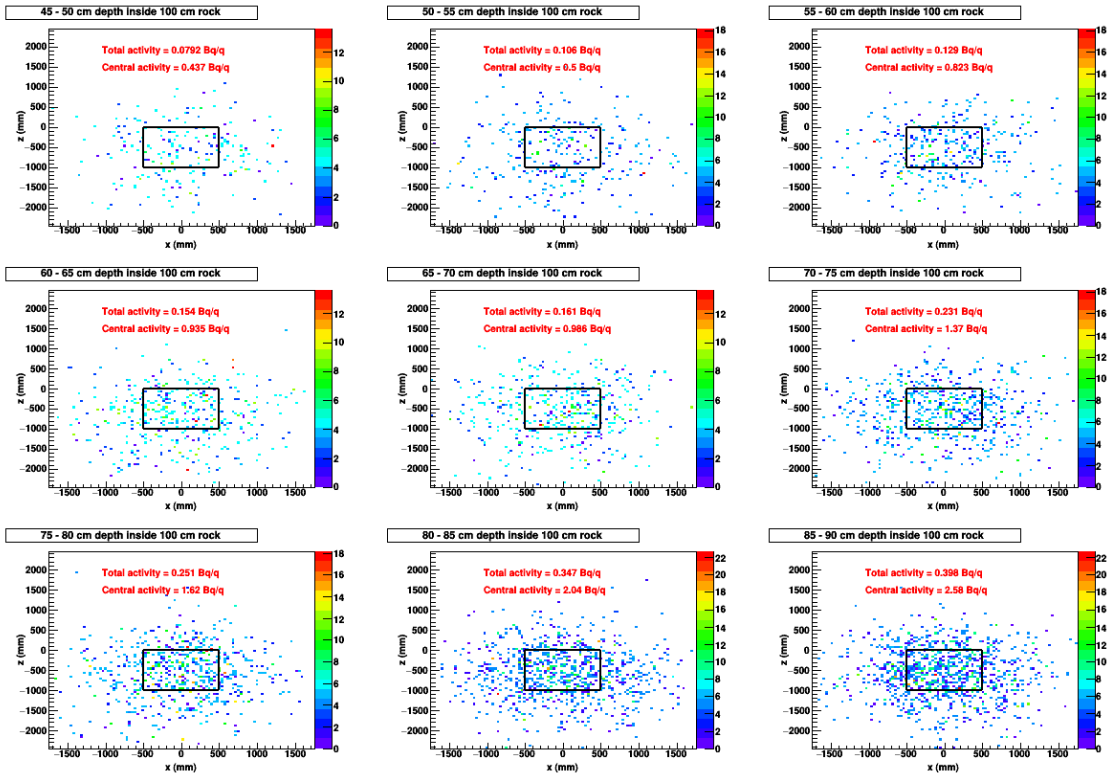


Figure 13. Spatial distribution of induced activity in the upper layers of the considered rock sample (45-90 cm) for the 40 cm steel and 80 cm boron concrete shielding.The overall activity in the layers is above the required limit of 0.1 Bq/g.

As rock activation studies ultimately evaluate the effectiveness of the shielding, a 2 m shielding consisting of 1 m of steel and 1 m of boron concrete was considered for calculations of the induced activation in the rock layers. The neutron spectra out of the reflector and out of the 2 m shielding is shown in Fig. 14. This plot also shows the neutron spectra out of the 4 m shielding side towards the KamLAND detector that will be placed between the target and the detector to suppress the neutron and gamma background (Fig. 9). The 2 m shielding decreases the neutron rates from 2.65×10^{-2}neutrons/POT (out of the reflector) to 6.86×10^{-10}neutrons/POT. With this extra shielding, the activation levels on central spots in the rock layers will also decrease significantly as Fig. 15 shows for the first 10 cm of rock situated in the proximity of the shielding.

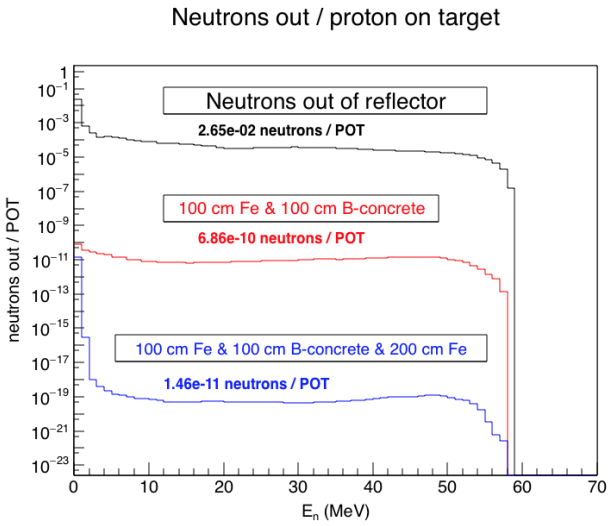


Figure 14. The neutron spectra out of the reflector and out of the 2 m shielding. It also shows the neutron spectra for the 4 m shielding side that fills the available space between the target system and the KamLAND detector (Fig. 9).

The total activity and the activity on the central hotspots for each layer of rock sample was calculated for the 200 cm shielding and the results are shown in Table 5.

6.5 Activity induced in the rock

The total activity in the entire rock sample considered after 5 years run and 2 years beam cool down period is shown in Fig. 16 with the peak value representing the activity at the beam switch off time. It can be seen that, for the 200 cm of shielding materials, the induced activity inside the rock is well below the imposed limit of 0.1 Bq/g, both throughout the beam on period, as well as after the beam switch off.

6.6 Distribution of Isotope Production with Rock Height

At the rock surface the slow neutrons will be responsible for surface activation, but faster neutrons will also produce activation at higher levels inside the rock. The isotope production inside the rock varies with the distance from the top layer of shielding. A large fraction of isotopes are produced

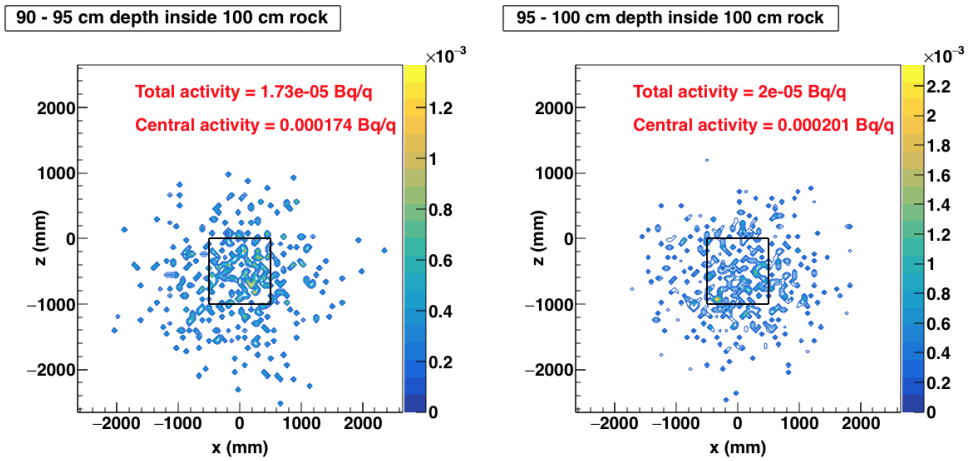


Figure 15. Spatial distribution of induced activity in the lowest layers of the considered rock sample, in the close proximity of the target and shielding system (90-100 cm). The overall activity in the layers is below the required limit of 0.1 Bq/g even in the central hotspots. This analysis is for the 200 cm shielding.

Table 5. The total and central activity on hotspots in each layer of the rock

Rock layer (cm)	Total activity: $10^{-6}(Bq/g)$	Central activity: $10^{-5}(Bq/g)$
0-5	0.116	0.113
5-10	0.407	0.113
10-15	0.663	0.175
15-20	0.856	0.917
20-25	0.84	1.04
25-30	0.859	0.661
30-35	1.10	1.07
35-40	1.48	1.02
40-45	2.4	1.42
45-50	2.5	2.53
50-55	3.25	2.97
55-60	3.89	3.36
60-65	5.01	4.3
65-70	5.87	4.53
70-75	8.28	6.54
75-80	8.94	9.4
80-85	12.5	10.9
85-90	13.4	10.5
90-95	17.3	17.4
95-100	20	20.1

in close proximity of target-shielding system with the production decreasing with the rock height and reaching a minimal value after 1 m of rock.

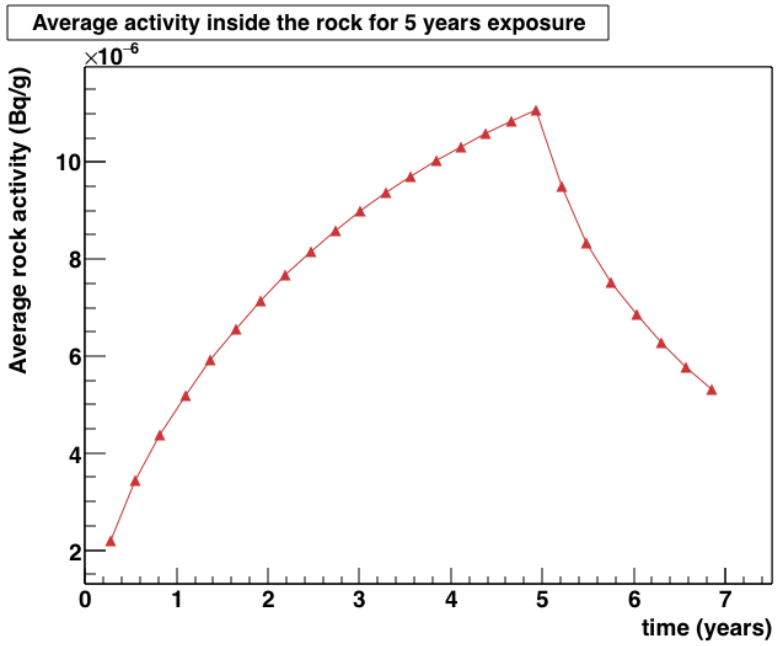


Figure 16. The total averaged activity in the entire rock during beam On and beam Off time. The total shielding thickness is 200 cm.

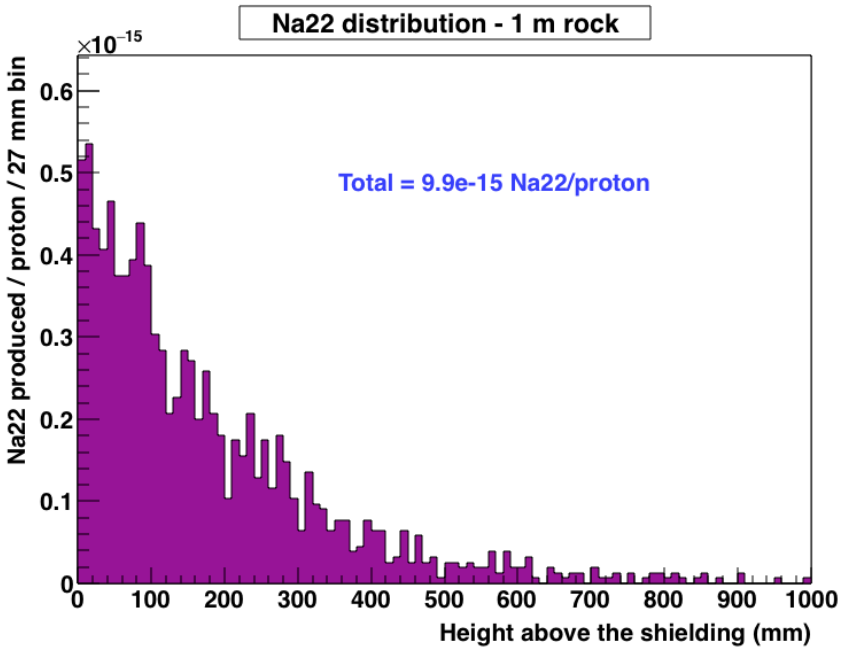


Figure 17. ^{22}Na production as a function of rock height for the 200 cm shielding (100 cm steel and 100 cm boron concrete).

The ^{22}Na production as a function of rock height is shown in Fig. 17. As ^{22}Na is a significant component of the rock chemical composition, even a small flux of high energy neutrons can contribute to an unacceptable high ^{22}Na production.

7. Shielding Requirements for Reducing the Neutron and Photon Physics Backgrounds in the KamLAND Detector

While the majority of non-beam backgrounds for IsoDAR at KamLAND can be experimentally measured and subtracted by comparing beam-on versus beam-off measurement periods, there are a few backgrounds inherent to the beam and target itself that must be accounted for. Most significant of these are neutrons produced by the interaction of the proton beam on the Li-Be target. Many of these neutrons will be captured on the ^{7}Li, which will then decay to produce the electron antineutrinos that are to be measured in the experiment, but there is a significant portion that will not. Geant4 simulations find that approximately 2.65×10^{-2} neutrons per proton-on-target (POT) will escape the neutrino-producing reflector and enter the target shielding. Due to the calculated 7.88×10^{24} POT over IsoDAR's five year run, this represents an unacceptably high background of neutrons into the KamLAND detector that the needs to be reduced through shielding.

IsoDAR will study two kinds of neutrino events during its run. The first are inverse beta decay (IBD) events, of which there will be 8.2×10^5 events over the five year run. These events are characterized by a prompt positron signal with $E_{vis} = E_{\bar{\nu}_e} - 0.78$ MeV coincident with a delayed neutron capture releasing a 2.2 MeV gamma within 200 μs. These events will not be affected by the neutron background since the signal is a two-part delayed coincidence. The second kind of event to be studied is the sample of low-energy $\bar{\nu}_e$-electron scatters (ES). There will be approximately 2600 of these events above a 3 MeV threshold over the five year run, and they will be easily mimicked by elastic scatters of neutrons in the KamLAND detector. Thus, additional shielding is needed to reduce the rate of neutrons and gammas over 3 MeV in the KamLAND detector region to a rate less than about 200 over the five year run.

7.1 Neutron Shielding

7.1.1 Target Shielding

The IsoDAR target is already shielded by 200 cm of material intended to absorb neutrons in order to comply with Japan's radiation requirements for the surrounding cavern. A full Geant4 simulation from the incoming POT to the neutrons escaping from this shielding showed a final output of just 6.86×10^{-10} neutrons per POT, which drops to 5.40×10^{-10} above the 3 MeV threshold. The majority of these neutrons are oriented away from the KamLAND detector due to the geometry of the target shielding, with many escaping through the vacuum of the beam pipe or the less heavily shielded water access tubes. Additional shielding is placed outside the target cube to further shield these accesses in the interests of radiation reduction, and also helpfully prevents the majority of these neutrons from moving towards the detector.

After the target shielding and accounting for the limited solid angle intercepted by the KamLAND detector, the incoming neutron flux towards the KamLAND detector is reduced to 1.069×10^{-9} neutrons above 3 MeV per POT. This estimate is made after a full simulation starting from incoming beam protons at 60 MeV through the entire target geometry, and then counting the neutrons whose direction of motion will intercept the detector itself, with the assumption that neutrons will scatter as much out of the intercepting solid angle as into it. This assumption allows us to use straight line trajectories for neutrons leaving the target region for the purposes of estimating neutron flux in the detector.

7.1.2 Additional Shielding Design

The additional shielding will be placed between the IsoDAR target and the KamLAND detector complex, and will be composed of stacked blocks of steel to produce a solid rectangle 2 m thick, 5 m high, and 5 m wide. This shielding block will be slightly off center from the target, with center around 50 cm downstream from the center of IsoDAR. This is because simulations of the full IsoDAR target from POT to escaping neutrons show that the majority of high energy neutrons, that the shielding block is meant to moderate, escape on the downstream end of the target (See Fig. 18).

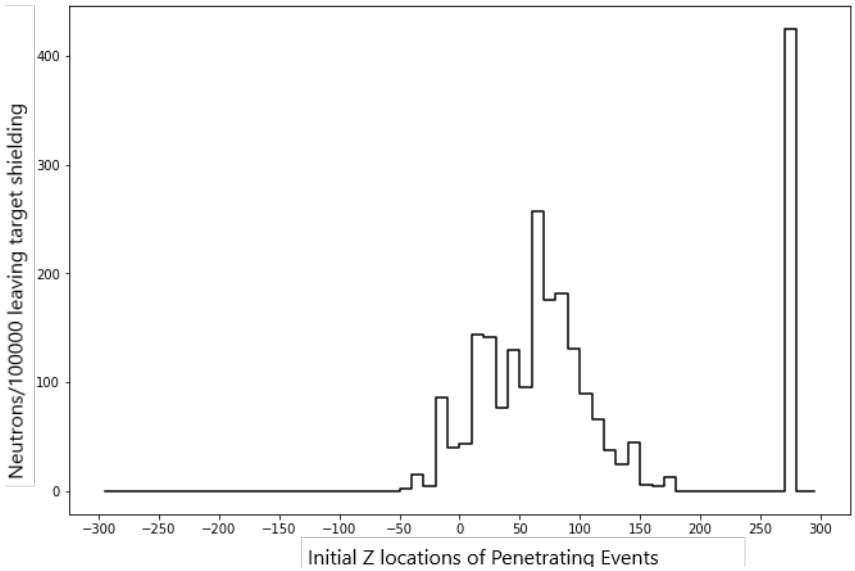


Figure 18. The initial z (along the beam direction with positive downstream) locations of a sample of the neutron events which successfully passed through the KamLAND shielding during the first round of simulation (without the additional 2m of iron). The large spike on the far right represents the excess of neutrons escaping the shielding through the water cooling pipes, which shall be countered by a downstream shift of the additional shielding.

This is due to the water cooling pipes on that end, which provide neutrons an easier path out of the shielding. Unlike the beam pipe on the upstream end, which provides a similar function, these pipes are not encased in additional shielding blocks, so a shift of the additional shielding will be necessary to prevent an excess of neutrons from that end. Fortunately, there is a demonstrated lack of penetrating events from the upstream end which enables this shift without increasing the neutron background by any significant amount.

7.1.3 KamLAND Buffer Region and Additional Shielding

Further simulations were based on the neutron energy and direction spectra out of the target shielding and focused on the effectiveness of the KamLAND buffer region in reducing the incoming neutron flux. Unfortunately, while the KamLAND buffer region, at minimum 100 cm of water and 250 cm of paraffin oil, is very effective at capturing and moderating lower energy neutrons less

than 10 MeV, it is comparatively far less effective on higher energy neutrons greater than 30 MeV. Incoming neutrons with energy greater than 50 MeV would enter the detector with energy above the threshold of 3 MeV at rates above 1×10^{-3} per neutron, i.e. for every neutron above 50 MeV entering the KamLAND buffer region there will be at least 1×10^{-3} neutrons above 3 MeV entering the detector. This resulted in background rates several orders of magnitude above that desired, with a total above 3 MeV of 5.92×10^{-17} neutrons per POT. Given the 7.88×10^{24} POT over the 5 year run this yields a total background of 4.66×10^{8} neutrons.

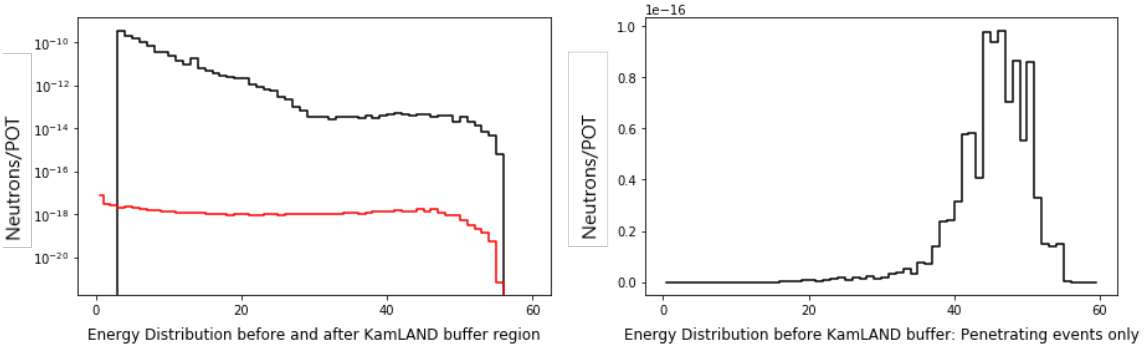


Figure 19. The above left shows the neutron energy distributions (in MeV) before (black) and after (red) the KamLAND buffer region without any additional shielding. The right plot shows the energy distribution of the penetrating neutrons only, i.e. the neutrons that reach the detector with energy > 3 MeV.

These studies demonstrated the need for additional shielding to be added in the 2 m space between the edge of KamLAND and the outer layer of the target shielding. Further, they allowed the prioritization of moderating or slowing high energy neutrons rather than all neutrons in this shielding, as seen in Fig. 19. As different materials have different moderating effects on different energies of neutrons, this was very useful. Iron was selected as the material of choice in this shielding layer due to its high effective cross section for neutrons between 20 and 60 MeV, the energy domain for penetrating neutrons.

As demonstrated in Fig. 20, the addition of 2m of iron shielding (bringing the total to 4 m) between the end of the target shielding and the start of the KamLAND buffer region drops the penetrating neutrons by nearly 8 orders of magnitude, especially in the higher energy domains where the buffer region proved insufficient. All combined, this total shielding left an estimated 2.78×10^{-24} neutrons per POT above the 3 MeV threshold in the KamLAND detector region, which is sufficient to meet our requirements. This represents a mere 22 neutrons above 3 MeV in KamLAND over the entire 5 year run.

This estimate is further taken to be conservative due to the overestimation inherent in the two part simulation, which was made with a rounded up energy distribution to start the second part. IsoDAR will also benefit from beam timing checks that can be used to reduce slow neutron plus energy analyses of the final events. The final neutron distribution in the detector region is essentially homogenous from 3 to 55 MeV, while the ES signal events peak around 10 MeV and do not exceed 20 MeV, as this is the maximum neutrino energy from the ^{8}Li decays.

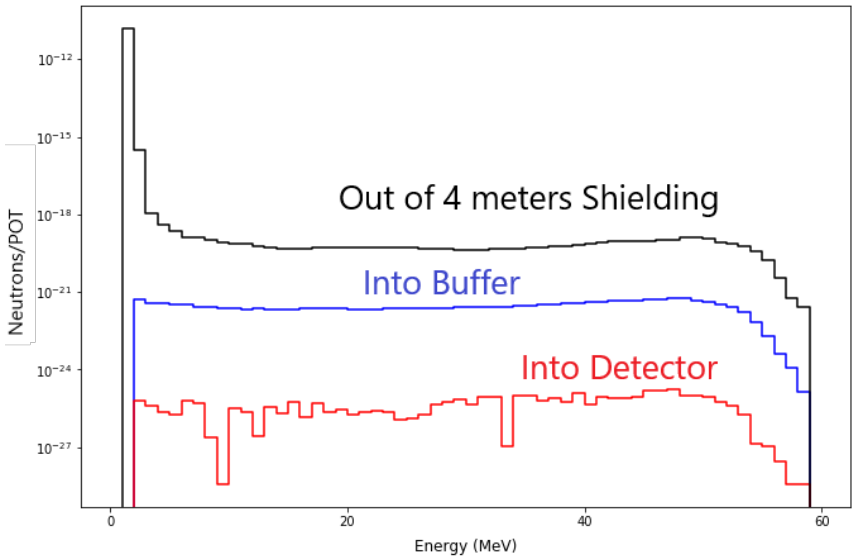


Figure 20. The displayed neutron energy distributions are taken from the simulation of the full geometry of the KamLAND detector and buffer. The simulation started with the neutron energy distribution out of the target and additional 2 m shielding (giving 4m total shielding) (black) and ended with the neutron energy distribution entering into the detector (red), with an intermediate energy check at the transition between the water and mineral oil buffer layers (blue).

7.2 Photon background

The same steel shielding also suppresses the gamma background towards KamLAND. As stated before, the shielding was designed asymmetrically, having a larger thickness towards the detector (4 m) with the extra 2 m filling the space between target and detector. For detector background studies only the neutrons having an energy above 3 MeV are of concern since ES signal to be detected is above 3 MeV. The total number of gammas with energies above 3 MeV that enter the KamLAND detector in a solid angle of 0.17π is 3.26×10^{-25} gammas/POT. These gammas are produced mainly by neutron inelastic processes (3.17×10^{-25}gammas/POT) but at smaller rates also by neutron capture (7.36×10^{-27}gammas/POT). (See Fig. 21). Photon inelastic processes and radioactive decay give a less significant contribution to the total number of gammas. Low energy gammas are produced also in proton inelastic, deuteron inelastic, ion inelastic, alpha inelastic and photon nuclear processes, apart from the ones mentioned above (Fig. 22).

The gamma background is calculated to be 2.38×10^{-24} gammas/POT with energies above 3 MeV and is produced in the detector mainly by inelastic interactions on carbon (2.31×10^{-24} gammas/POT) and at a smaller rate by neutron capture on hydrogen (5.69×10^{-26} gammas/POT) with a peak energy of 2.2 MeV. For 4 m of shielding towards the detector, the total numbers of gammas above 3 MeV is 2.7×10^{-24} gammas/POT. Therefore, for 7.88×10^{24}protons/5 years run, this corresponds to ≈ 22 gammas above 3 MeV for the 5 years experiment.

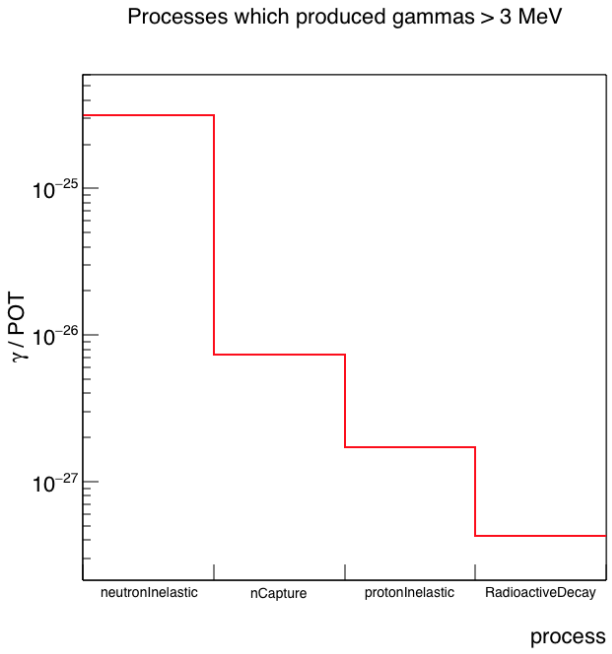


Figure 21. The gammas with energies above 3 MeV that enter the Kamland detector are produced in the buffer regions mainly by neutron inelastic processes. Other processes like neutron capture, proton inelastic and radioactive decay have a lower contribution.

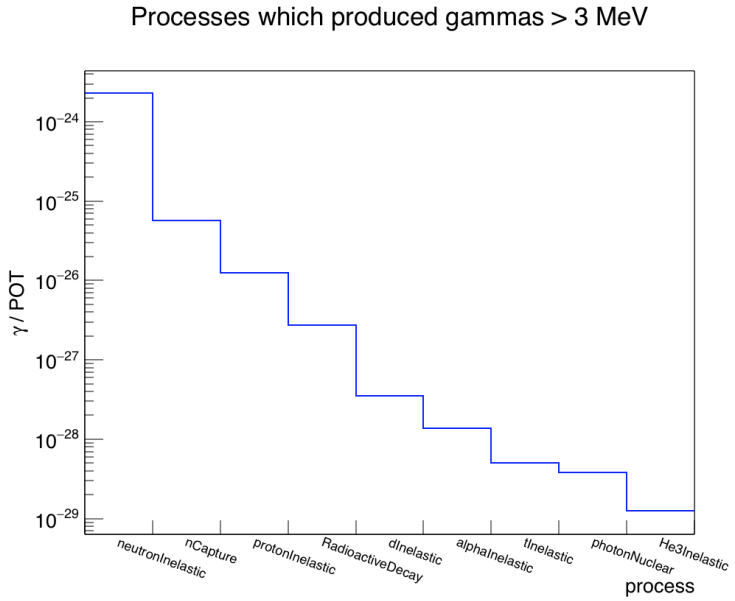


Figure 22. Rate of processes that produce gammas with energies above 3 MeV for various particle interactions inside the Kamland detector. Apart from neutron inelastic, neutron capture, proton inelastic and radioactive decay, other processes that give a measurable contribution are deuteron, alpha, triton and He3 inelastic processes, and photon nuclear processes.

8. Conclusion

A shielding system for the IsoDAR neutrino experiment was designed to meet the neutron flux irradiation requirements out of the shielding with a limiting value of $10^{-13} n/p/mm^2$. This value was obtained from neutron irradiation of the Kamioka rock samples and analysis of the radionuclides that were produced. New materials developed at Jefferson Laboratory like boron concrete together with layers of steel were used to design the shielding in the confined space of the current location in the mine, without significant rock excavation. The radionuclides produced in the rock were identified and the ones that give a significant contribution to the total induced activation were the long lived isotopes like ^{60}Co, ^{22}Na, ^{152}Eu, and ^{154}Eu. A spatial distribution of the activity on the cavern wall identified the hot spots and the activity for these spots is below the required limitation of 0.1 Bq/g after 5 years run plus 2 years cool down period for a 2 m shielding. The neutron and gamma physics backgrounds in the KamLAND detector were simulated for the 5 years experiment and it was found that the levels at which they are produced are not a significant background for detecting the IBD and ES physics signals.

Acknowledgements

Adriana Bungau, Jose Alonso and Janet Conrad are supported by NSF PHY 1912764 and Larry Bartoszek, Edward Dunton and Michael Shaevitz are supported by NSF PHY 1707969. We thank Susan Kayser for the editorial support of this paper.

References

[1] KamLAND - Kamioka Liquid Scintillator Antineutrino Detector, http://www.awa.tohoku.ac.jp/kamlande.

[2] IAEA Safety Standards Series, RS-G-1.7, Radiation Safety Guide, 2004.

[3] M. Abs et al., "IsoDAR@KamLAND: A Conceptual Design Report for the Technical Facility", arXiv: 1511.05130.

[4] IsoDAR collaboration, "IsoDAR@KamLAND: A Conceptual Design Report for the Conventional Facilities", arXiv: 1710.09325.

[5] T. N. S. A. Group, Recommendations to the Department of Energy and the National Science Foundation on a Future U.S. Program in Neutrino Oscillations, arXiv: http://www.science.doe.gov/hep/hepap_reports.shtm.

[6] T. P. Panel, "Report of the Particle Physics Project Prioritization Panel", [arXiv: http://www.er.doe.gov/hep/hepap_reports.shtm].

[7] LSND collaboration, "Evidence for neutrino oscillations from the observation of anti-neutrino (electron) appearance in an anti-neutrino (muon) beam", Phys.Rev. D 64 (2001) 112007 [hep-ex/0104049].

[8] MiniBooNE collaboration, "Improved Search for $\bar{\nu}_\mu \to \bar{\nu}_e$ Oscillations in the MiniBooNE Experiment, Phys. Rev. Lett. 110 (2013) 161801 [arXiv: 1303.2588].

[9] G. Mention, M. Fechner, T. Lasserre, T.A. Mueller, D. Lhuillier, M. Cribier et al., "The Reactor Antineutrino Anomaly", Phys.Rev. D 83 (2011) 073006 [arXiv: 1101.2755].

[10] J.M. Conrad, M.H. Shaevitz, "Multiple Cyclotron Method to Search for CP-violation in the Neutrino Sector", Phys. Rev. Lett. 104 (2010) 141802 [arXiv:0912.4079].

[11] J.M. Conrad, M.H. Shaevitz, I. Shimizu, J. Spitz, M. Toups and L. Winslow, "Precision $\bar{\nu}_e$-electron scattering measurements with IsoDAR to search for new physics", Phys. Rev. D 89 (2014) 072010 [arXiv: 1307.5081].

[12] S. Abe et al., KamLAND Collaboration, Phys. Rev. Lett. 100, 221803 (2008).

[13] A. Bungau, J. Alonso, L. Bartoszek, J. Conrad, M. Shaevitz and J. Spitz, "Optimizing the ^8Li yield for the IsoDAR Neutrino Experiment", Journal of Instrumentation, vol.14, (2019) [arXiv:1805.00410v1].

[14] IsoDAR@KamLAND: A Conceptual Design Report for the Technical Facility, Kamland, September 2015.

[15] https://www.jlab.org/news/stories/new-shielding-designed-put-block-neutrons

[16] M. B. Chadwick et al., "ENDF/B-VII.1 nuclear data for science and technology: Cross sections, covariances, fission product yields and decay data", Nucl. Data Sheets, 112 (2011) 2887.

[17] A. J. Koning et al., "TENDL-2014: TALYS-based evaluated nuclear data library", https://www.talys.eu/tendl-2014.html.

[18] www.talys.eu/fileadmin/talys/user/docs/talys1.4.pdf

[19] T. Nakagawa et al., "Japanese Evaluated Nuclear Data Library Version 3 Revision-2: JENDL-3.2", J. Nucl. Sci. Technol. 32 (1995) 1259.

[20] Yu. N. Shubin et al., "Cross section data library MENDL-2 to study activation and transmutation of materials irradiated by nucleons of intermed. energies", INDC(CCP)-385, International Atomic Energy Agency (1995).

[21] J. P. Wellisch, "Geant4 physics validation for large HEP detectors", Nucl. Instrum. Meth. A 502 (2003) 669.

[22] F Waterman *et al.*, 1979, Medical Physics, vol 6, p432.

[23] S Johnsen, 1977, Medical Physics, vol 4, p255.

[24] H Almos *et al.*, 1977, Medical Physics, vol 4, p486.

[25] M Meier *et al.*, 1989, Nuclear Science and Engineering, vol 102, p310.

[26] P Heintz *et al.*, 1977, Medical Physics, vol 4, p250.

[27] R Madey *et al.*, 1977, Medical Physics, vol 4, p322.

[28] G Harrison *et al.*, 1980, Medical Physics, vol 7, p348.

[29] M Osipenko *et al.*, 2013, Nuclear Instruments and Methods, A 723, p8.

[30] I. Tilquin, P. Froment, M. Cogneau, Th. Delbar, J. Vervier and G. Ryckewaert, "Experimental measurements of neutron fluxes produced by proton beams (23 - 80 MeV) on Be and Pb targets", Nucl. Instrum. Meth. A 545 (2005) 339.

[31] mcnpx-lanl.gov

[32] S. Abe *et all.*, 2010, Phys. Rev C 81, 025807.

[33] A. Tang, G. Horton-Smith, V. A. Kudryavtsev and A. Tonazzo, 2006, Phys. Rev. D 74, 053007.

[34] L. Winslow, "First Solar Neutrinos from KamLAND: A Measurement of the ^{8}B Solar Neutrino Flux", University of California, Berkley, 2008.